A Generic and Efficient E-field Parallel Imaging Correlator for Next-Generation Radio Telescopes

Nithyanandan Thyagarajan,[1]* Adam P. Beardsley,[1] Judd D. Bowman[1]
and Miguel F. Morales[2]

[1]*Arizona State University, School of Earth and Space Exploration, Tempe, AZ 85287, USA*
[2]*University of Washington, Department of Physics, Seattle, WA 98195, USA*

ABSTRACT
Abstract here (250 words)

Key words: instrumentation: interferometers – techniques: image processing – techniques: interferometric

1 INTRODUCTION

Radio astronomy is entering an era in which interferometers of hundreds to thousands of individual antennas are needed to achieve desired survey speeds. Nowhere is this more apparent than at radio frequencies below 1.4 GHz. The study of the history of hydrogen gas throughout the universe's evolution is pushing technology development towards arrays of low-cost antennas with large fields of view and densely packed apertures. Similarly, the search for transient objects and regular monitoring of the time-dependent sky is driving instruments in the same direction. A number of new telescopes are under development around the world based on this new paradigm, including the Murchison Widefield Array (MWA, Tingay et al. 2013), the Precision Array for Probing the Epoch of Reionization (PAPER, Parsons et al. 2010), the Hydrogen Epoch of Reionization Array (HERA [1]), the LOw Frequency ARray (LOFAR, de Vos et al. 2009), the Canadian Hydrogen Intensity Mapping Experiment (CHIME, Bandura et al. 2014), the Long Wavelength Array (LWA, Ellingson et al. 2013), and the low frequency component of the Square Kilometer Array Low Frequency Aperture Array (SKA-Low Mellema et al. 2013).

This paradigm shift requires a fundamentally new approach to the design of digital correlators (Lonsdale et al. 2000). Modern correlators calculate the cross-power correlation between all antenna pairs in many narrow frequencies, forming *visibilities*, the traditional fundamental measurement of radio interferometers. The computational requirements for a modern FX correlator scale with the number of antenna pairs, or the square of the number of antennas $\sim N_{\mathrm{ant}}^2$ (Bunton 2004). For this reason traditional correlators have difficulty scaling to thousands of antennas. As an example, the full HERA correlator for 352 dishes with 200 MHz of bandwidth requires 212 trillion complex multiplies and adds per second (TMACS). Future arrays with thousands of collecting elements will require orders of magnitude more computation, making the correlator the dominant cost.

For certain classes of radio arrays there is an alternative to the FX correlator that can lower the computational burden by directly performing a spatial fast Fourier transform (FFT) on the electric fields measured by each antenna in the array at each time step, removing the cross-correlation step. This relieves the computational scaling from the harsh N_{ant}^2 to the more gentle envelope of $N_{\mathrm{pix}} \log N_{\mathrm{pix}}$, where N_{pix} is the number of pixels in the Fourier transform (e.g. Morales 2011; Tegmark & Zaldarriaga 2009; Tegmark & Zaldarriaga 2010). This architecture is often referred to as a "direct imaging" correlator because it eliminates the intermediary cross- correlation data products of the FX and earlier lag correlators, but instead directly forms images from the electric field measurements.

Direct imaging correlators have begun to be explored on deployed arrays including the Basic Element for SKA Training II (BEST-2) array (Foster et al. 2014), the Omniscope (Zheng et al. 2014), and an earlier incarnation at higher frequencies with the intent of pulsar timing (Otobe et al. 1994; Daishido et al. 2000). However, each of these examples make assumptions about the redundancy of the array layout, and require the collecting elements are identical. On the other hand, the MOFF algorithm achieves the same $N_{\mathrm{pix}} \log N_{\mathrm{pix}}$ computational scaling without placing any restriction on antenna placement, can accommodate non-identical beam patterns, and is a provably optimal mapping (Morales 2011). This algorithm uses the antenna beam patterns to grid the electric field measurements to a regular grid in the software holography/A-transpose fashion (Morales & Matejek 2009; Bhatnagar, S. et al. 2008; Tegmark 1997a) before performing the spatial FFT. This process has been shown to theoretically produce a data product identical to images produced from the traditional FX correlator.

Here we present the first software implementation of the MOFF correlator, and announce the public release of the E-field Parallel Imaging Correlator (EPIC) code. We begin with a technical description of the algorithm in §2, then discuss our particular implementa-

---

* E-mail: t_nithyanandan@asu.edu
[1] http://reionization.org

tion in §3. We then verify the output data quality from our code in §4 by presenting simulated images from both the EPIC correlator and comparing to a simulated FX correlator. We also demonstrate the performance with real-world data from the LWA. In §5 we analyze the scaling relationships of the algorithm. We identify specific array design classes where the EPIC correlator is computationally more efficient than the FX algorithm. We conclude and discuss future research prospects in §6.

2   MATHEMATICAL FRAMEWORK

We provide a quick summary of the mathematical equivalence of the MOFF and FX correlators detailed in Morales (2011).

Electric fields from astrophysical sources, $E(\hat{\mathbf{s}})$, in the sky coordinate system denoted by unit vector $\hat{\mathbf{s}}$ propagate towards the observer as:

$$\widetilde{E}(\mathbf{r}) = \int E(\hat{\mathbf{s}}) \, e^{-i2\pi\mathbf{r}\cdot\hat{\mathbf{s}}} \, \mathrm{d}^2\hat{\mathbf{s}}, \tag{1}$$

where, $\mathbf{r}$ denotes the observer's coordinate system and $\widetilde{E}(\mathbf{r})$ is the propagated electric field. Thus the propagated electric field is a linear superposition of the electric fields emanating from astronomical sources with appropriate complex phases. It can also be described as a Fourier transform of the electric fields in the sky coordinates.

An antenna, a, measures a phased sum of these propagated electric fields over its effective collecting area with an additive receiver noise:

$$\widetilde{E}_a = \int \widetilde{W}_a(\mathbf{r} - \mathbf{r}_a) \, \widetilde{E}(\mathbf{r}) \, \mathrm{d}^2\mathbf{r} + \widetilde{n}_a \tag{2}$$

$$= \int \widetilde{W}_a(\mathbf{r} - \mathbf{r}_a) \left[\int E(\hat{\mathbf{s}}) \, e^{-i2\pi\mathbf{r}\cdot\hat{\mathbf{s}}} \, \mathrm{d}^2\hat{\mathbf{s}} \right] \mathrm{d}^2\mathbf{r} + \widetilde{n}_a \tag{3}$$

$$= \int \delta(\mathbf{r} - \mathbf{r}_a) \left[\int W_a(\hat{\mathbf{s}}) \, E(\hat{\mathbf{s}}) \, e^{-i2\pi\mathbf{r}\cdot\hat{\mathbf{s}}} \, \mathrm{d}^2\hat{\mathbf{s}} \right] \mathrm{d}^2\mathbf{r} + \widetilde{n}_a \tag{4}$$

where, $\widetilde{W}_a(\mathbf{r})$ is the aperture electric field illumination pattern of the antenna and its Fourier transform, $W_a(\hat{\mathbf{s}})$ is the directional antenna voltage response.

Interferometers measure *visibility* – the degree of coherence – between electric fields measured by a pair of antennas (van Cittert 1934; Zernike 1938; Thompson et al. 2001). Visibility, $\widetilde{V}_p$, can be written as:

$$\widetilde{V}_p = \left\langle \widetilde{E}_a \widetilde{E}_b^\star \right\rangle \tag{5}$$

$$= \int \delta(\mathbf{u} - \mathbf{u}_p) \left[\int e^{-i2\pi\mathbf{u}\cdot\hat{\mathbf{s}}} B(\hat{\mathbf{s}}) I(\hat{\mathbf{s}}) \, \mathrm{d}^2\hat{\mathbf{s}} \right] \mathrm{d}^2\mathbf{u} + n_p, \tag{6}$$

where, $I(\hat{\mathbf{s}})$ is the sky brightness, $B(\hat{\mathbf{s}})$ is the antenna power response, $\mathbf{u}$ denotes the coordinates of the *uv*- measurement plane, $\mathbf{u}_p \equiv \mathbf{r}_a - \mathbf{r}_b$ is the antenna spacing vector corresponding to the antenna pair p, and n_p is the receiver noise. This signifies that the visibility ($\widetilde{V}_p$) measured between a pair of antennas (p) is obtained by the multiplying the sky brightness $I(\hat{\mathbf{s}})$ by the antenna power response $B(\hat{\mathbf{s}})$ and Fourier transform from the directional coordinates ($\hat{\mathbf{s}}$) to *uv* coordinates, which are then sampled at the locations of the antenna spacings (or baselines), namely, $\mathbf{u}_p$ using the sampling function $\delta(\mathbf{u} - \mathbf{u}_p)$ and added to the receiver noise n_p. This can be

equivalently re-written as:

$$\widetilde{V}_p = \int \delta(\mathbf{u}' - \mathbf{u}_p) \left[\int \tilde{B}(\mathbf{u}' - \mathbf{u}) \right.$$
$$\left. \times \left[\int e^{-i2\pi\mathbf{u}\cdot\hat{\mathbf{s}}} I(\hat{\mathbf{s}}) \, \mathrm{d}^2\hat{\mathbf{s}} \right] \mathrm{d}^2\mathbf{u} \right] \mathrm{d}^2\mathbf{u}' + n_p, \tag{7}$$

where, $\tilde{B}(\mathbf{u})$ denotes the *uv*-space antenna power response obtained by a Fourier transform of $B(\hat{\mathbf{s}})$. Effectively, the multiplication in image space by $B(\hat{\mathbf{s}})$ has been replaced by a convolution with $\tilde{B}(\mathbf{u})$ in *uv*-space. This is the software holographic equivalent of traditional FX correlator output. Following the matrix notation of Morales (2011), the above equation can be expressed as:

$$\mathbf{m}(\mathbf{v}) = \widetilde{B}(\mathbf{v}, \mathbf{u}) \, \mathbf{F}(\mathbf{u}, \hat{\mathbf{s}}) \, I(\hat{\mathbf{s}}) + \mathbf{n}(\mathbf{v}), \tag{8}$$

where, the sky brightness $I(\hat{\mathbf{s}})$ is Fourier transformed using $\mathbf{F}(\mathbf{u}, \hat{\mathbf{s}})$ and the resultant spatial coherence function is weighted and summed using the antenna power response, $\widetilde{B}(\mathbf{v}, \mathbf{u})$ in *uv*-space sampled at the baseline location to obtain the measured visibilities:

$$\mathbf{m}(\mathbf{v}) = \left\langle \widetilde{E}(\mathbf{a}) * \widetilde{E}(\mathbf{a}') \right\rangle_t . \tag{9}$$

$\mathbf{m}(\mathbf{v})$ denotes visibilities measured by cross-correlating measured antenna electric fields over all possible pairs of $\mathbf{a}$ and $\mathbf{a}'$. It is the same as equation 5 written in matrix notation.

Using the optimal map-making formalism (Tegmark 1997b; Tegmark 1997a), a software holography image is formed using (Morales & Matejek 2009):

$$I'(\hat{\mathbf{s}}) = \mathbf{F}^{\mathrm{T}}(\hat{\mathbf{s}}, \mathbf{u}) \, \widetilde{B}^{\mathrm{T}}(\mathbf{u}, \mathbf{v}) \, \mathbf{N}^{-1} \, \mathbf{m}(\mathbf{v}) \tag{10}$$

where the measured visibilities are weighted by the inverse of the system noise, following a gridding process using the holographic antenna power response as the gridding kernel followed by a Fourier transform to create an image $I'(\hat{\mathbf{s}})$ which is the optimal estimate of the true image $I(\hat{\mathbf{s}})$.

It may be noted that the antenna power response in *uv*-plane can be written as:

$$\tilde{B}_p(\mathbf{u}) = \widetilde{W}_a(\mathbf{u}) * \widetilde{W}_b^\star(\mathbf{u}) \tag{11}$$

where, $W_a(\mathbf{u})$ and $W_b(\mathbf{u})$ denote the individual antenna voltage responses. Thus $\tilde{B}_p(\mathbf{u})$ is a cross-correlation of the individual antenna voltage responses. Similarly, it can be shown that

$$\left\langle E(\hat{\mathbf{s}}) \, E^\star(\hat{\mathbf{s}}') \right\rangle = \left\langle E(\hat{\mathbf{s}}) \, E^\star(\hat{\mathbf{s}}') \delta(\hat{\mathbf{s}} - \hat{\mathbf{s}}') \right\rangle$$
$$= \left\langle |E(\hat{\mathbf{s}})|^2 \right\rangle = I(\hat{\mathbf{s}}) \tag{12}$$

From equations 2, 7, 9, 11 and 12, the optimal image in equation 10 can be expressed equivalently as:

$$I'(\hat{\mathbf{s}}) = \left\langle \left| \mathbf{F}^{\mathrm{T}}(\hat{\mathbf{s}}, \mathbf{r}) \, \widetilde{\mathbf{W}}^{\mathrm{T}}(\mathbf{r}, \mathbf{a}) \, \widetilde{\mathbf{N}}(\mathbf{a}, \mathbf{a}) \, \widetilde{E}(\mathbf{a}) \right|^2 \right\rangle_t . \tag{13}$$

The term inside the angular brackets before squaring has a very similar form as that in equation 10. It signifies that the measured antenna electric fields are weighted by the antenna noise, weighted and gridded by the antenna aperture kernel, Fourier transformed and finally squared to obtain the same image estimated that would have been obtained using equation 10.

Equations 13 and 10 are identical to each other obtained as a consequence of the multiplication-convolution theorem of Fourier transforms. In other words, equation 10 is obtained by a Fourier transform of the gridded spatial correlation of electric fields measured by antennas while equation 13 is obtained by squaring the Fourier transform of the gridded electric fields measured by the antennas. The time-scale of averaging in equations 5 and 13 is set

by the coherence time-scale of the electric fields or the science requirement (e.g., timescale of variability or transients).

There are some important differences between the two techniques:

(i) The time-averaging cannot be performed on a stochastic measurement but only on its statistical properties. In FX imaging, the visibilities measured between antenna pairs represent spatial correlations which can be time-averaged following which the they gridded and imaged. However, in MOFF imaging both antenna and gridded electric fields are stochastic and therefore have to be imaged before time-averaging.

(ii) In FX imaging, electric fields measured on antennas are not correlated with themselves and hence lack zero spacing measurements. In contrast, in MOFF imaging, since the gridded electric fields are imaged and squared, they contain information from auto-correlated electric fields at zero spacing. Hence, they have to be subtracted from the images.

3 SOFTWARE IMPLEMENTATION

We have implemented the MOFF imaging technique in our "E-field Parallel Imaging Correlator" – a highly parallelized Object Oriented Python package, [2] now publicly available. Besides implementing the MOFF imaging algorithm it also includes FX imaging using software holography technique and a simulator for generating electric fields from a sky model.

Figure 1 shows the flowchart for MOFF imaging. The propagated electric fields are shown on the left at different time stamps, $t_1 \ldots t_M$. At each time stamp, the electric fields measured by antennas are denoted by $E_1(t) \ldots E_N(t)$. The F-engine performs a temporal Fourier transform on the electric field time-series to obtain electric field spectra $E_1(f) \ldots E_N(f)$ ($\widetilde{E}_a$ in matrix notation) for each of the antennas. Each of the complex antenna gains are calibrated to correct the corresponding electric field spectra. These calibrated electric fields are gridded using an antenna-based gridding convolution function following which it is spatially Fourier transformed and squared to obtain images for every time stamp. These images are then time-averaged to obtain the accumulated image $I(f)$ ($I(\hat{\mathbf{s}})$ in matrix notation).

Figure 2 shows the flowchart for software holographic imaging from a FX correlator. The antenna-based F-engine is identical to that in the MOFF processing. The electric field spectra each antenna are then cross- multiplied in the X-engine with those from all other antennas to obtain the visibilities $V_{\mathrm{ij}}(f)$ ($\mathbf{m}(\mathbf{v})$ in matrix notation). They are calibrated and time-averaged to obtain $\langle V_{\mathrm{ij}}(f) \rangle$ which are then gridded and imaged to obtain the image $I(f)$. The $I(f)$ obtained from both techniques are identical as explained in §2.

Here, we discuss the components of these architectures in detail.

3.1 Temporal Fourier transform

This module is common to the MOFF and FX imaging techniques. Time samples of electric fields measured by the antenna and digitized by the A/D converter is Fourier transformed to generate electric field spectra. This step can be parallelized by antennas as shown in Figure 3. The output is then fed to either MOFF and FX imaging pipelines.
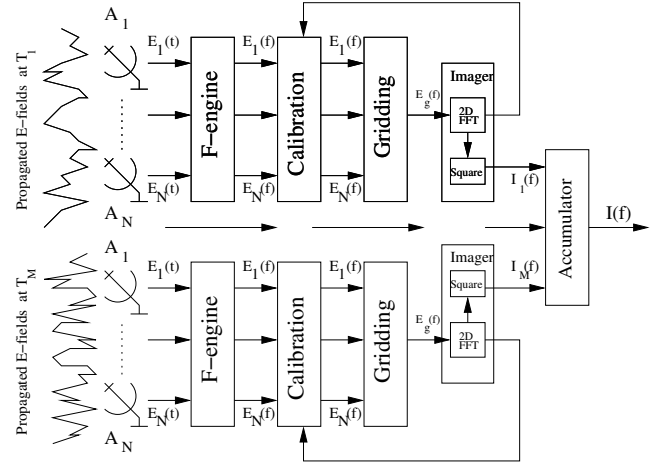
Figure 1. A flowchart of MOFF imaging in EPIC. The propagated electric fields shown on the left are measured as time-series $E_1(t) \ldots E_N(t)$ by the antennas which are then Fourier transformed by the F-engine to produce electric field spectra $E_1(f) \ldots E_N(f)$. They are calibrated and gridded. The gridded electric fields $E_g(f)$ from each time series are imaged to produce an images $I_1(f) \ldots I_N(f)$. These images are time-averaged to obtain the final image $I(f)$.
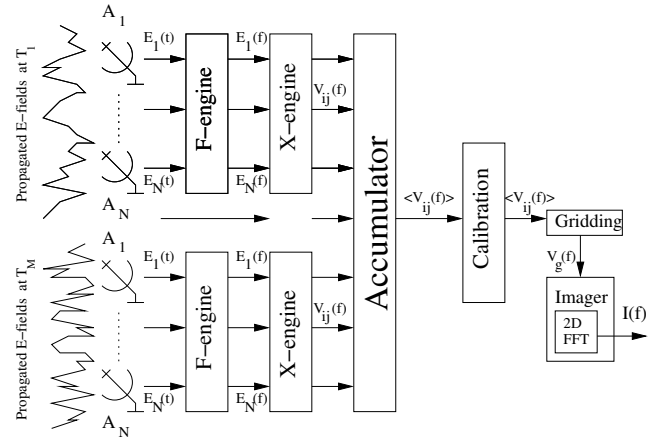

Figure 2. A flowchart of FX imaging in EPIC. The FX process flow shares the F-engine with the MOFF process. Following the F-engine, the electric fields pass through the X-engine to obtain visibilities $V_{\mathrm{ij}}(f)$ which are calibrated and time-averaged. Then they are gridded to obtain the gridded visibilities $V_g(f)$ which are then imaged to obtain the image $I(f)$.
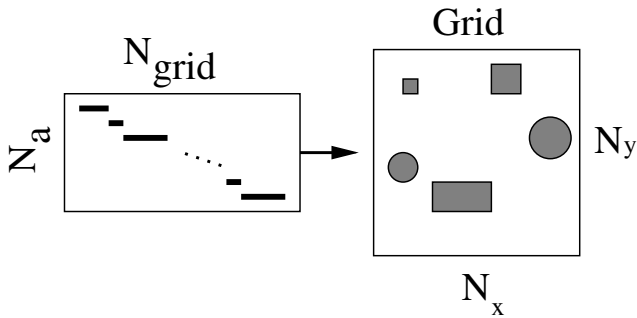
3.2 Antenna-to-Grid Mapping

A grid is generated on the coordinate system in which antenna locations are specified with a grid spacing that is at most $\lambda_{\min}/2$ even at the highest frequency to ensure there is no aliasing even from regions of the sky far away from the field of view. The number of locations on the grid is restricted to be a power of 2.

The gridding kernel in the simplest case is given by the antenna aperture illumination function, $\widetilde{B}(\mathbf{r} - \mathbf{r}_a)$, which can specified either by a functional form or as a table of values against locations around the antennas. A nearest neighbor mapping from all antenna footprints to grid locations is created using an efficient k-d tree algorithm (Maneewongvatana & Mount 1999). There is no restric-
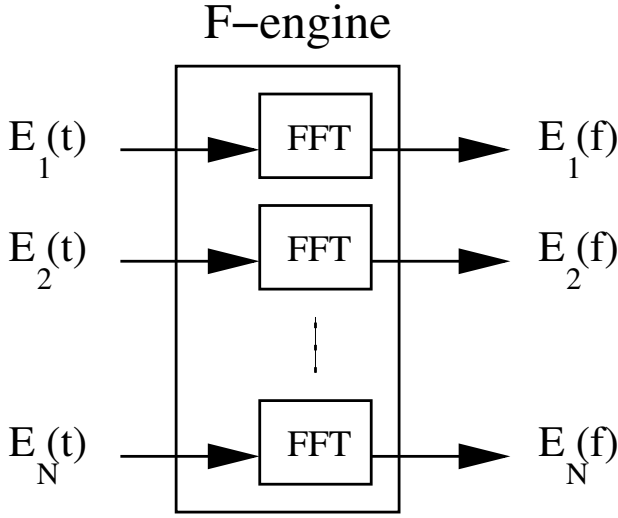
F–engine

Figure 3. Block diagram of a F-engine. The electric field data streams from antennas are Fourier transformed in parallel to generate electric field spectra.

Figure 4. Block diagram of an antenna-to-grid mapping. A sparse block-diagonal matrix of total size $N_{\text{grid}} \times N_{\text{a}}$ is created where each block contains roughly the number of pixels covered by the respective kernel. The antenna aperture illumination kernels do not have to be identical to each other. A discrete set of arbitrarily placed antennas are now placed onto a regular grid.

tion here that the aperture illumination function has to be identical across antennas.

In the most general case, this gridding kernel could contain information on the w-projection effect, and even other time-dependent ionospheric effects. For a stationary antenna array in the absence of any time-dependent effects, this mapping has to be determined only once in the antenna array coordinate frame. The antenna-to-grid mapping matrix, $\mathbf{M}(\mathbf{r}, \mathbf{e})$ is described as a transformation matrix from the space of measured electric fields ($\mathbf{e}$) to the antenna array grid denoted by $\mathbf{r}$. Since each antenna occupies a footprint typically the size of its aperture, $\mathbf{M}(\mathbf{r}, \mathbf{e})$ which is generally of size $N_{\text{grid}} \times N_{\text{a}}$, reduces to a sparse block-diagonal matrix with only N_{a} blocks and roughly N_{k} non-zero entries per block. Figure 4 illustrates the antenna-to-grid mapping matrix and the grid containing the mapped aperture footprints of the antennas.

3.3 Calibration

3.4 Gridding Convolution

The antenna array aperture illumination over the entire grid, $\widetilde{W}(\mathbf{r})$, is obtained by a projection of the individual antenna aperture illuminations:

$$\widetilde{W}(\mathbf{r}) = \sum_a \widetilde{W}_a(\mathbf{r} - \mathbf{r}_a) \tag{14}$$

$$= \mathbf{M}(\mathbf{r}, \mathbf{e})\, \mathcal{I}(\mathbf{e}), \tag{15}$$

where, $\mathcal{I}(\mathbf{e})$ is a row of ones. This is achieved using efficient multiplication with the sparse matrix created in the antenna-to-grid mapping process. Unless $\widetilde{W}(\mathbf{r})$ includes time-dependent effects of the ionosphere or the instrument, it needs to be computed just once for the entire observation. However, the gridding of electric fields must be computed at every readout of the electric field spectra. Thus,

$$\widetilde{E}(\mathbf{r}) = \mathbf{M}(\mathbf{r}, \mathbf{e})\, E(\mathbf{e}), \tag{16}$$

where, $E(\mathbf{e})$ denotes the spectra of measured antenna electric fields.

In practice the grid is set to be a power of 2 such that the grid spacing is at most $\lambda/2$ even at the highest frequency in the observing band.

3.5 Spatial Fourier Transform

Before the spatial Fourier transform, the gridded electric fields are padded with zeros in order to match the grid size and angular size of each image pixel that would have been obtained with software holography of output from an FX correlator.

In MOFF imaging, these are spatially Fourier transformed followed by a squaring operation at every timestamp for every frequency channel. In FX imaging, the spatial Fourier transform is performed only once per integration timescale and does not include a squaring operation.

3.6 Time-averaging

In MOFF imaging, the measured antenna electric fields and the corresponding holographic electric field images are zero-mean stochastic quantities. Hence, they cannot be time-averaged to reduce noise. The statistical quantity stable with time in this case are the square of the holographic electric field images. Thus, squared images have to be formed at every instant of time before averaging as indicated in equation 13.

In contrast, visibilities measured by an antenna are statistically stable within an integration time interval. Hence, they are averaged after calibration as shown in equation 5. It is advantageous to average them in visibilities before imaging because visibilities represent a compact representation of the information in images. Hence it is more computationally efficient to average antenna pair visibilities rather than images. Since this averaging has been performed already on the visibilities over an integration timescale, the imaging step has to be performed only once per integration cycle. FX imaging holds this advantage as long as the square of the number of antennas is smaller than the number of pixels on the image.

4 VERIFICATION

We use the EPIC simulator to generate electric field samples from a sky model. In our example, we use 16 frequency channels each
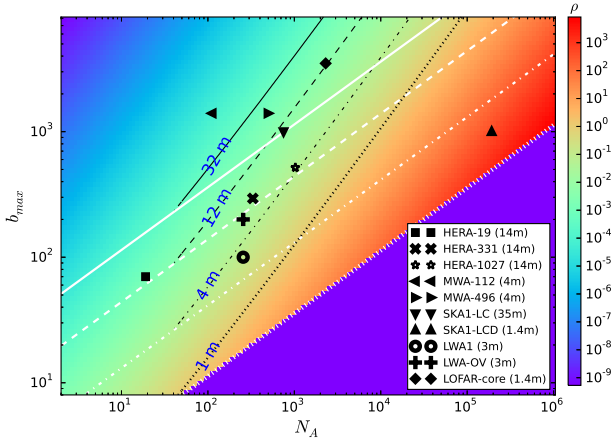
Figure 5. Current and instruments planned for future in parameter space of baseline length and number of antennas with MOFF and FX.
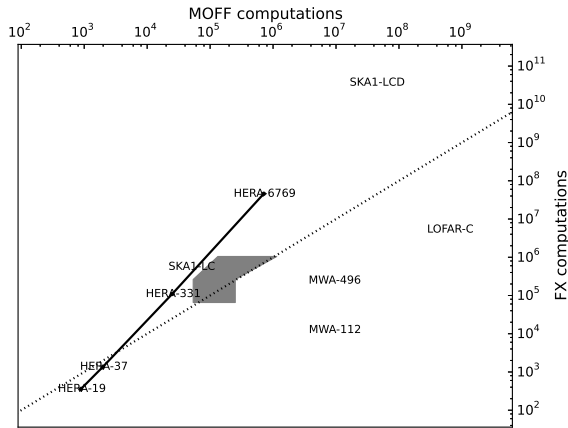
Figure 6. Current and instruments planned for future in parameter space of number of complex multiplies and adds with MOFF and FX.

of width δf =100 kHz, 10 point sources of random flux densities at random locations. The number of timestamps in one integration cycle was kept at four where each A/D timeseries is $1/\delta f = 10\,\mu$s long.

Show examples using simulations

Discuss PSF differences due to slight differences arising out of gridding

Apply it on LWA data

5   ANALYSIS AND FEASIBILITY

5.1   Scaling Relations: MOFF vs. FX

5.2   Scaling Up

5.3   Case Study

6   CONCLUSIONS

ACKNOWLEDGEMENTS

REFERENCES

Bandura K., et al., 2014, in Society of Photo-Optical Instrumentation Engineers (SPIE) Conference Series. p. 22 (arXiv:1406.2288), doi:10.1117/12.2054950

Bhatnagar, S. Cornwell, T. J. Golap, K. Uson, J. M. 2008, A&A, 487, 419

Bunton J. D., 2004, Experimental Astronomy, 17, 251

Daishido T., et al., 2000, Proc. SPIE, 4015, 73

Ellingson S. W., et al., 2013, IEEE Transactions on Antennas and Propagation, 61, 2540

Foster G., Hickish J., Magro A., Price D., Zarb Adami K., 2014, Monthly Notices of the Royal Astronomical Society, 439, 3180

Lonsdale C. J., Doeleman S. S., Cappallo R. J., Hewitt J. N., Whitney A. R., 2000, in Butcher H. R., ed., Society of Photo-Optical Instrumentation Engineers (SPIE) Conference Series Vol. 4015, Radio Telescopes. pp 126–134

Maneewongvatana S., Mount D. M., 1999, eprint arXiv:cs/9901013,

Mellema G., et al., 2013, Experimental Astronomy, 36, 235

Morales M. F., 2011, PASP, 123, 1265

Morales M. F., Matejek M., 2009, MNRAS, 400, 1814

Otobe E., et al., 1994, PASJ, 46, 503

Parsons A. R., et al., 2010, The Astronomical Journal, 139, 1468

Tegmark M., 1997a, Phys. Rev. D, 55, 5895

Tegmark M., 1997b, ApJ, 480, L87

Tegmark M., Zaldarriaga M., 2009, Phys. Rev. D, 79, 083530

Tegmark M., Zaldarriaga M., 2010, Phys. Rev. D, 82, 103501

Thompson A. R., Moran J. M., Swenson Jr. G. W., 2001, Interferometry and Synthesis in Radio Astronomy, 2nd Edition. Wiley

Tingay S. J., et al., 2013, PASA - Publications of the Astronomical Society of Australia, 30

Zernike F., 1938, Physica, 5, 785

Zheng H., et al., 2014, MNRAS, 445, 1084

de Vos M., Gunst A., Nijboer R., 2009, Proceedings of the IEEE, 97, 1431

van Cittert P. H., 1934, Physica, 1, 201

APPENDIX A: SOME EXTRA MATERIAL

If you want to present additional material which would interrupt the flow of the main paper, it can be placed in an Appendix which appears after the list of references.

This paper has been typeset from a TEX/LATEX file prepared by the author.